Numerical modelling of spontaneous slab breakoff dynamics during continental collision

CYRILL BAUMANN[1]*, TARAS V. GERYA[1,2] & JAMES A. D. CONNOLLY[1]

[1]*Department of Geosciences, Swiss Federal Institute of Technology (ETH-Zurich), CH-8092 Zurich, Switzerland*

[2]*Geology Department, Moscow State University, 119899 Moscow, Russia*

*Corresponding author (e-mail: baumancy@ethz.ch)

Abstract: Slab detachment or breakoff is directly associated with phenomena like morphological orogenesis, occurrence of earthquakes and magmatism. At depth the detachment process is slow and characterized by viscous rhelogy, whereas closer to the surface the process is relatively fast and plastic. Using a 2D mantle model 1500 km deep and 4000 km wide we investigated, with finite-difference and marker-in-cell numerical techniques, the impact of slab age, convergence rate and phase transitions on the viscous mode of slab detachment. In contrast to previous studies exploring simplified breakoff models in which the blockage responsible for inducing breakoff is kinematically prescribed, we constructed a fully dynamic coupled petrological–thermomechanical model of viscous slab breakoff. In this model, forced subduction of a 700 km-long oceanic plate was followed by collision of two continental plates and spontaneous slab blocking resulting from the buoyancy of the continental crust once it had been subducted to a depth of 100–124 km. Typically, five phases of model development can be distinguished: (a) oceanic slab subduction and bending; (b) continental collision initiation followed by the spontaneous slab blocking, thermal relaxation and unbending – in experiments with old oceanic plates in this phase slab roll-back occurs; (c) slab stretching and necking; (d) slab breakoff and accelerated sinking; and (e) post-breakoff relaxation.

Our experiments confirm a correlation between slab age and the time of spontaneous viscous breakoff as previously identified in simplified breakoff models. The results also demonstrate a non-linear dependence of the duration of the breakoff event on slab age: a positive correlation being characteristic of young (<50 Ma) slabs while for older slabs the correlation is negative. The increasing duration of the breakoff with slab age in young slabs is attributed to the slab thermal thickness, which increases both the slab thermal relaxation time and duration of the necking process. In older slabs this tendency is counteracted by negative slab buoyancy, which generate higher stresses that facilitate slab necking and breakoff. A prediction from our breakoff models is that the olivine–wadsleyite transition plays an important role in localizing viscous slab breakoff at depths of 410–510 km due to the buoyancy effects of the transition.

Slab detachment or breakoff is directly associated with phenomena like morphological orogenesis, occurrence of earthquakes and magmatism. This process was hypothesized on the basis of gaps in hypocentral distributions and within tomographic images of subducted slabs (Isacks & Molnar 1969; Barazangi *et al.* 1973; Pascal *et al.* 1973; Chung & Kanamori 1976; Fuchs *et al.* 1979), and is supported both by theoretical considerations (Sacks & Secor 1990; Davies & von Blanckenburg 1995; von Blanckenburg & Davies 1995) and detailed seismic tomography (Spakman *et al.* 1988; Wortel & Spakman 1992, 2000; Xu *et al.* 2000; Levin *et al.* 2002). Slab detachment is often attributed to a decrease in subduction rate subsequent to continental collision (e.g. Davies & von Blanckenburg 1995; Wong A Ton & Wortel 1997), an effect caused by the buoyancy of the continental lithosphere that is introduced into the subduction zone.

In addition to multiple geophysical, geological and geochemical investigations acknowledging slab detachment as a possible explanation for observations in various regions (Andrews & Billen 2009 and references therein), analytical models and laboratory and numerical experiments have been undertaken to characterize the breakoff process (e.g. Davies & von Blanckenburg 1995; Larsen *et al.* 1995; Yoshioka *et al.* 1995; Yoshioka & Wortel 1995; Wong A Ton & Wortel 1997; Pysklywec *et al.* 2000; Chemenda *et al.* 2000; Buiter *et al.* 2002; Gerya *et al.* 2004*b*; Faccenda *et al.* 2006, 2008; Mishin *et al.* 2008; Ueda *et al.* 2008; Zlotnik *et al.* 2008; Andrews & Billen 2009).

Recent thermomechanical numerical models indicate two modes of detachment (Andrews & Billen 2009): (1) deep *viscous detachment* that is characteristic of strong slabs (maximum yield strength ≥500 MPa), and is controlled by thermal

relaxation (heating) of the slab and subsequent thermomechanical necking in dislocation creep regime (Gerya *et al.* 2004*b*; Faccenda *et al.* 2008; Zlotnik *et al.* 2008); and (2) relatively fast, shallow *plastic detachment* characteristic of weak slabs (maximum yield strength ≤ 300 MPa) and controlled by plastic necking of the slab (Mishin *et al.* 2008; Ueda *et al.* 2008; Andrews & Billen 2009). Andrews & Billen (2009) demonstrated that the time before the onset of viscous detachment increases with slab age, indicating that detachment time is controlled by the thickness and integrated stiffness of the thermally relaxing slabs (Gerya *et al.* 2004*b*). In contrast, the plastic detachment time is independent of age and is controlled by the rate of flow of the surrounding mantle (Andrews & Billen 2009).

Two-dimensional dynamic models of viscous detachment have shown that, following the cessation of subduction, necking of the slab and detachment occur after 8–30 Ma at a depth of 150–400 km (Gerya *et al.* 2004*b*; Faccenda *et al.* 2008; Andrews & Billen 2009). In numerical experiments with viscous dissipation included (Gerya *et al.* 2004*b*) shear heating in the necking area causes slab breakoff to occur 8% faster than in models that neglect viscous dissipation (Gerya *et al.* 2004*b*). Therefore, the slab necking process is not purely mechanical. Zlotnik *et al.* (2008) modelled the influence of mantle phase transitions on the viscous slab detachment and demonstrated that the olivine–spinel transition facilitates the detachment by increasing the negative buoyancy of the hanging slab.

Thermomechanical models of plastic detachment indicate shallower (Andrews & Billen 2009) and even near-surface (Mishin *et al.* 2008; Ueda *et al.* 2008) depths of breakoff. The timing and location of plastic failure is controlled by the dynamics of the loading of the subducting plate by negatively buoyant slab during or shortly after the active phase of convergence. Such models have also shown that, in the case of multiple plates, shallow slab breakoff can affect plate dynamics causing processes such as subduction flip and re-initiation (Mishin *et al.* 2008).

Thermomechanical numerical studies of breakoff (Gerya *et al.* 2004*b*; Zlotnik *et al.* 2008; Andrews & Billen 2009) explored a simplified static breakoff model with two fixed oceanic plates and a kinematically prescribed interruption of subduction. Thus, no dynamic thermomechanical model of this process accounting for the presence of the continental plates and cessation of subduction (e.g. Chemenda *et al.* 2000; Faccenda *et al.* 2008) has been studied. The absence of such an effort leaves a gap in our understanding of dynamics and controls of breakoff. In particular, prescribed slab blocking does not allow for the proper balance between the slab

strength, geometry (length, inclination) and negative buoyancy, and may create unrealistic geodynamic situations (e.g. heavy slabs that are too weak to remain coherent during subduction). The simplified models also fail to reproduce the thermal and lithological structure of the collisional orogen that forms in response to continental subduction (e.g. Chemenda *et al.* 2000; Burov *et al.* 2001; Faccenda *et al.* 2008). Therefore, in this paper we investigate the dynamics, geometry and duration of viscous detachment of oceanic slabs after cessation of active oceanic–continental subduction due to collision between two continental plates by means of a high-resolution 2D numerical study. We will account for the effects of phase transformations as well as pressure-, temperature- and strain-rate-dependent rheology of the mantle and the subducted oceanic crust. Compared to previous studies dealing with thermomechanical detachment experiments (e.g. Gerya *et al.* 2004*b*; Zlotnik *et al.* 2008; Andrews & Billen 2009), our petrological–thermomechanical model is fully dynamic and considers the presence of the colliding continental plates as causing subduction blocking and breakoff.

Model set-up and governing equations

Initial configuration

To investigate slab breakoff we developed a 2D, coupled petrological–thermomechanical numerical model of oceanic–continental subduction followed by collision (Fig. 1) using the I2VIS code (Gerya & Yuen 2003*a*). The spatial co-ordinate frame of the model is 4000×1500 km. The non-uniform 774×106 rectangular grid is designed with a resolution varying from 2×2 km in the studied subduction–collision–breakoff zone to 30×50 km far from it (Fig. 1b). Lithological structure of the model is represented by a grid of around 3 million randomly distributed active Lagrangian markers used for advecting various material properties and temperature. The density of the marker distribution varies from 1 marker km^{-2} in the high-resolution zone to 0.25 marker km^{-2} far from it. The oceanic crust consists of a 3 km-thick basaltic layer underlain by a 5 km-thick gabbroic layer. The continental crust consists of a 35 km-thick granodioritic layer.

The velocity boundary conditions are free slip at all boundaries except the lower boundary of the model domain, which is permeable in the vertical direction (Gerya *et al.* 2008*b*). An infinite-ike external free slip condition ($\partial v_x / \partial z = 0$, $\partial v_z / \partial z = v_z / \Delta z_{\text{external}}$, where v_x and v_z are, respectively, horizontal and vertical velocity components) along the bottom implies that free slip condition ($\partial v_x / \partial z = 0$, $v_z = 0$) is satisfied at an external boundary located at a certain depth $\Delta z_{\text{external}}$
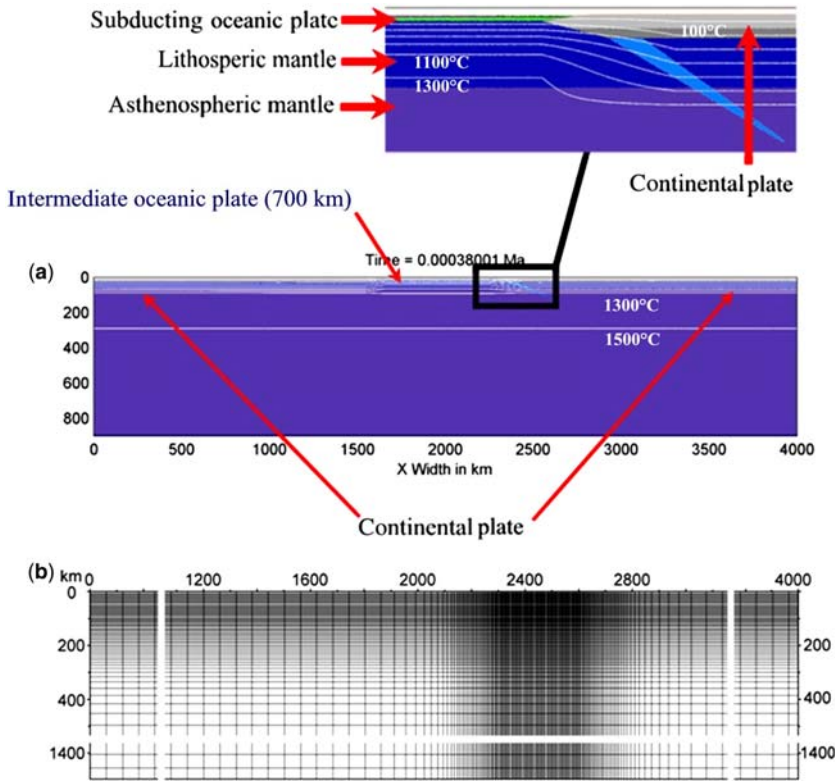
Fig. 1. Initial model set-up (**a**) and numerical grid (**b**) for conducted experiments. The flow law and petrological model of lithospheric and asthenospheric mantle are the same (Table 1); different colours are used for better visualization of slab dynamics. White lines are isotherms taken from 100 °C with 200 °C steps.

below the actual lower boundary of the model ($\Delta z_{external} = 1500$ km for the present study). Similar to the usual free slip condition, external free slip allows global conservation of mass in the computational domain. The top surface of the crust is calculated dynamically as an internal free surface by using initially a 10–12 km-thick deformable top layer (10 km over the continents and 12 km over the oceanic plate) with low viscosity (10^{19} Pa s) and density (1 kg m^{-3} for the atmosphere, above $z = 11$ km sea-water level, 1000 kg m^{-3} for the hydrosphere, below $z = 11$ km sea-water level, where z is the vertical co-ordinate taken downwards from the top of the model). The validity of the weak layer approach for approximating the free surface has recently been tested and proven (Schmelling *et al.* 2008) with the use of a large variety of numerical techniques (including our I2VIS code) and comparison with analogue modelling. The interface between this weak layer and the top of the oceanic crust deforms spontaneously and is treated as an internal erosion–sedimentation surface that evolves according to the transport equation solved at each time step

(Gerya & Yuen 2003*b*):

$$\frac{\partial z_{es}}{\partial t} = v_z - v_x \frac{\partial z_{es}}{\partial x} - v_s + v_e$$

where z_{es} is a vertical position of the surface as a function of the horizontal distance x; v_z and v_x are the vertical and horizontal components of material velocity vector at the surface; v_s and v_e are, respectively, sedimentation and erosion rates. As demonstrated by Pysklywec (2006) and Gerya *et al.* (2008*b*) in the case of subduction and collision variations in erosion–sedimentation rates may significantly affect crustal mass flux and consequently alter the behaviour of the crust–mantle interface. In the present paper we used moderate constant gross-scale erosion and sedimentation rates applicable for continental collision zones (Vance *et al.* 2003; Gerya *et al.* 2008*b*), which correspond to the relation:

$v_s = 0$ mm year^{-1}, $v_e = 1$ mm year^{-1} when $z < 9$ km (i.e. for ≥ 2 km elevation above the sea-water level)

$v_s = 1$ mm year^{-1}, $v_e = 0$ mm year^{-1} when $z > 11$ km (i.e. below the sea-water level).

The influences of erosion–sedimentation rates on the geometry of collisional orogens in the post-subduction collision model similar to the one explored in our study are discussed by Gerya *et al.* (2008a).

Subduction is prescribed by the total convergence rate $R_T = R_R + R_L$, where R_R and R_L are locally imposed constant velocities for the right and the left plates, respectively. Moving continental plates have finite width and are detached from the model boundaries (Fig. 2). This convergence condition was applied for 700 km of forced subduction of the oceanic plate. After this time the model was allowed to evolve spontaneously. The subduction area is initiated by a 5–50 km-wide weak zone of hydrated mantle that cuts across the mantle lithosphere from the bottom of the crust down to 190 km depth. Taking into account the critical role of water for subduction initiation (Regenauer-Lieb *et al.* 2001), this zone is characterized by wet olivine rheology (Ranalli 1995) and a low plastic strength limit of 1 MPa (Table 1). With the advance subduction, this zone is replaced by weak upper oceanic crust, which is also characterized by low plastic strength (Table 1). This device implies that high-pressure fluids are present along the slab interface during subduction (e.g. Sobolev & Babeyko 2005; Gerya *et al.* 2008a).

The initial geotherm for the oceanic lithosphere is defined by a half-space cooling model (e.g. Turcotte & Schubert 2002; Fowler 2005) for the prescribed lithospheric age (Table 2). The initial thermal structure of the continental lithosphere corresponds to a typical continental geotherm (e.g. Turcotte & Schubert 2002): 0 °C at the surface and 1345 °C at 140 km depth. A gradual transition from the oceanic to the continental geotherm is prescribed over a 200 km-wide section on either side of the ocean–continent boundary (Fig. 1a). The geotherm for the mantle below the lithosphere is defined by a near-adiabatic temperature gradient of 0.46 K km^{-1}. Thermal boundary conditions are 0 °C at the upper boundary of the model; no-flux conditions exist at the vertical boundaries. An infinite-like external constant temperature condition along the lower boundary is implemented using the following limitation: $\partial T / \partial z = (T_{external} - T)/ \Delta z_{external}$, where $T_{external} = 2140$ °C is the temperature prescribed at the external boundary.

Petrological model

The stable mineralogy and physical properties for the various lithologies were computed using Perple_X (Connolly 2005) with free energy minimization as a function of pressure and temperature. For this purpose we adopted the Mie–Grueneisen formulation of Stixrude & Bukowinski (1990), with the parameterization of Stixrude & Lithgow-Bertelloni (2005) augmented for lower-mantle phases as described by Khan *et al.* (2006). This parameterization limits the chemical model to the CaO–FeO–MgO–Al$_2$O$_3$–SiO$_2$. The mantle is assumed to have a pyrolitic composition, for which the thermodynamic parameterization is adequate to reproduce the expected lower-mantle phase relations (Mishin *et al.* 2008). Application of the thermodynamic model to the basaltic and gabbroic composition of the oceanic crust is more problematic because phase equilibrium experiments (Irifune & Ringwood 1993; Irifune *et al.* 1994; Hirose & Fei 2002; Ono *et al.* 2005) suggest the existence of several high-pressure phases that are not included in our parameterization. In addition, the CaO–FeO–MgO–Al$_2$O$_3$–SiO$_2$ model excludes volatile oxides, notably K$_2$O and Na$_2$O, that are more significant in the subducted oceanic crust; as a consequence our model is likely to overestimate the basalt–pyrolite density contrast. To calibrate this effect we found that experimentally derived density estimates for K$_2$O–Na$_2$O–CaO–FeO–MgO–Al$_2$O$_3$–SiO$_2$ (Irifune & Ringwood 1993; Ono *et al.* 2005) were 1.7–2.3% below those calculated here. Accordingly, neutral buoyancy in the Earth's interior most probably corresponds to conditions at which our basalt–pyrolite density contrast is 1.02 ± 0.03. Our models therefore overestimate the role of density-induced slab-pull forces in subduction.
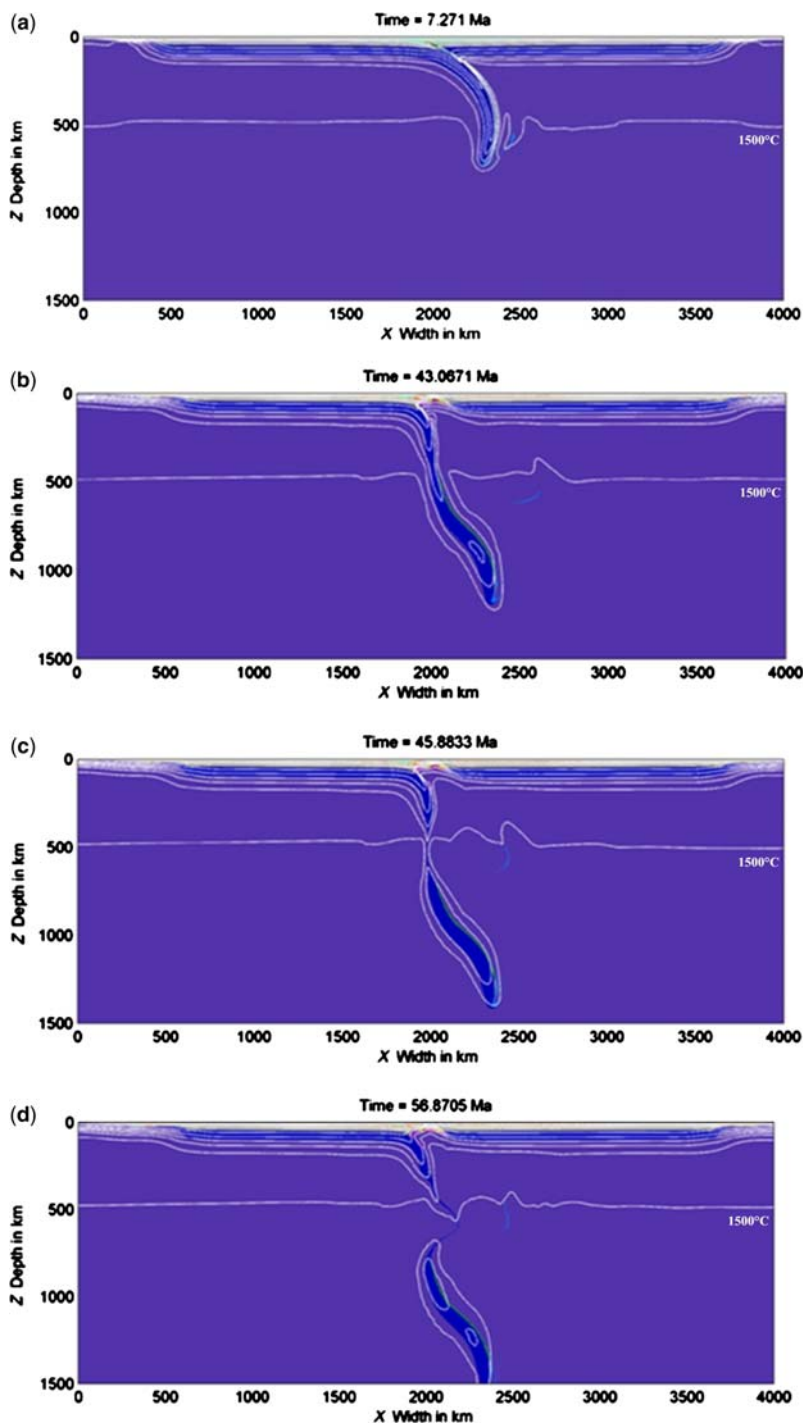
Thermomechanical model

The momentum, continuity and temperature equations for the 2D creeping flow, accounting for both thermal and chemical buoyancy, are solved using the I2VIS code based on conservative finite differences and non-diffusive marker-in-cell techniques (Gerya & Yuen 2003a). Conservation of mass is prescribed by the incompressible continuity equation:

$$\frac{\partial v_x}{\partial x} + \frac{\partial v_z}{\partial z} = 0.$$

The 2D Stokes' equations for creeping flow take the form:

$$\frac{\partial \sigma_{xx}}{\partial x} + \frac{\partial \sigma_{xz}}{\partial z} = \frac{\partial P}{\partial x}$$

$$\frac{\partial \sigma_{zz}}{\partial z} + \frac{\partial \sigma_{xz}}{\partial x} = \frac{\partial P}{\partial z} - g\rho(T, P, C, M).$$

Fig. 2. Reference model development (model cydd in Table 2). (**a**) Oceanic slab subduction and bending of the diving plate, high strength of the cold deeply subducted mantle lithosphere prevents its unbending and causes strong slab curvature (Gerya *et al.* 2008*b*); (**b**) thermal relaxation and unbending of the slab; (**c**) slab stretching and necking; (**d**) and slab breakoff and sinking. White lines are isotherms taken from 100 °C with 200 °C steps.

C. BAUMANN ET AL.

Table 1. *Material properties* used in 2D numerical experiments*

Material	H_r (μW m^{-3})	Standard density (ρ_0) (kg m^{-3})	Thermal conductivity (W m^{-1} K^{-1})	Rheology	$P-T$ conditions of wet solidus
Upper continental crust	1.0	2700 (solid) 2400 (molten)	$0.64 + \dfrac{807}{T + 77}$	Wet quartzite flow law, $c = 1$ MPa, $\sin(\varphi) = 0.15$	$889 + \dfrac{17900}{P + 54} + \dfrac{20200}{(P + 54)^2}$ at $P < 1200$ MPa, $831 + 0.06P$ at $P > 1200$ MPa
Lower continental crust	0.25	2800 (solid) 2400 (molten)	$0.64 + \dfrac{807}{T + 77}$	Plagioclase (An$_{75}$) flow law, $c = 1$ MPa, $\sin(\varphi) = 0.15$	$889 + \dfrac{17900}{P + 54} + \dfrac{20200}{(P + 54)^2}$ at $P < 1200$ MPa $831 + 0.06P$ at $P > 1200$ MPa
Upper oceanic crust (altered basalt)	0.25	3000 (solid) 2900 (molten)	$1.18 + \dfrac{474}{T + 77}$	Wet quartzite flow law, $c = 1$ MPa, $\sin(\varphi) = 0$	$973 - \dfrac{70400}{P + 354} + \dfrac{77800000}{(P + 354)^2}$ at $P < 1600$ MPa, $935 + 0.0035P + 0.0000062P^2$ at $P > 1600$ MPa
Lower oceanic crust (gabbro)	0.25	3000 (solid) 2900 (molten)	$1.18 + \dfrac{474}{T + 77}$	Plagioclase (An$_{75}$) flow law, $c = 1$ MPa, $\sin(\varphi) = 0.6$	$973 - \dfrac{70400}{P + 354} + \dfrac{77800000}{(P + 354)^2}$ at $P < 1600$ MPa, $935 + 0.0035P + 0.0000062P^2$ at $P > 1600$ MPa
Dry mantle (lithospheric and asthenospheric)	0.022	3300	$0.73 + \dfrac{1293}{T + 77}$	Dry olivine flow law, $c = 1$ MPa, $\sin(\varphi) = 0.6$	–
Mantle in the subduction initiation zone	0.022	3200	$0.73 + \dfrac{1293}{T + 77}$	Wet olivine flow law, $c = 1$ MPa, $\sin(\varphi) = 0$	–
References	Turcotte & Schubert 2002	Turcotte & Schubert 2002	Clauser & Huenges 1995	Chopra & Paterson 1981; Brace & Kohlstedt 1980; Ranalli 1995	Schmidt & Poli 1998; Poli & Schmidt 2002

*Other material properties (density, heat capacity, latent heating, thermal expansion) are computed from the petrological model by Gibbs energy minimization; for models without phase transitions and for the continental crust in all models the following properties are used: $C_p = 1000$ J kg^{-1} K^{-1}, $\rho = \rho_0[1 - \alpha(T - T_0)] \times [1 + \beta(P - P_0)]$, where $\alpha = 3 \times 10^{-5}$ K^{-1} is thermal expansion, $\beta = 1 \times 10^{-5}$ MPa^{-1} is compressibility, ρ_0 is standard density at $T_0 = 298$ K and $P_0 = 0.1$ MPa.

Table 2. *Description of the numerical experiments used in this work*

Run	Slab age (Ma)	Left plate rate (cm year^{-1})	Right plate rate (cm year^{-1})	Phase transitions
cyda	20	+05	−05	yes
cydb	40	+05	−05	yes
cydc (reference model)	60	+05	−05	yes
cydd (reference model)	80	+05	−05	yes
cyde	100	+05	−05	yes
cyaq	80	+10	0	yes
cyar	80	0	−10	yes
cyas	80	+03	−07	yes
cydh	40	+05	−05	no
cydi	60	+05	−05	no

The density $\rho\,(T, P, C, M)$ depends explicitly on the temperature (T), the pressure (P), the rock composition (C) and the mineralogy (M).

The Lagrangian temperature equation includes latent heat effects of phase transformations in the crust and mantle, and is formulated as (Gerya & Yuen 2003a):

$$\rho C_\mathrm{p}\left(\frac{DT}{Dt}\right) = -\frac{\partial q_x}{\partial x} - \frac{\partial q_z}{\partial z} + H_\mathrm{r} + H_\mathrm{T} + H_\mathrm{s}$$

$$q_x = -k(T, C)\frac{\partial T}{\partial x},$$

$$q_z = -k(T, c)\frac{\partial T}{\partial z}$$

$$C_\mathrm{p} = \left(\frac{\partial H}{\partial T}\right)_\mathrm{P}$$

$$H_\mathrm{T} = \rho\left[\frac{1}{\rho} - \left(\frac{\partial H}{\partial P}\right)_\mathrm{T}\right]\frac{DP}{Dt}$$

$$H_\mathrm{s} = \sigma_{xx}\dot{\varepsilon}_{xx} + \sigma_{zz}\dot{\varepsilon}_{zz} + \sigma_{xz}\dot{\varepsilon}_{xz}$$

where D/Dt is the substantive time derivative; x and z denote the horizontal and vertical co-ordinates, respectively; σ_{xx}, σ_{zz}, σ_{xz} are the components of the deviatoric stress tensor; $\dot{\varepsilon}_{xx}$, $\dot{\varepsilon}_{zz}$, $\dot{\varepsilon}_{xz}$ are the components of the strain rate tensor; P is the pressure; T is the temperature; q_x and q_z are the heat fluxes; ρ is the density; $k(T, c)$ is the thermal conductivity; C_p is the effective isobaric heat capacity, that is, incorporating latent heat; H is rock enthalpy; H_r, H_T and H_s denote radioactive heat production, the energetic effect of isothermal (de)compression and shear heating, respectively. To account for physical effects of phase transitions on the dynamics of breakoff (Zlotnik *et al.* 2008) we used the coupled petrological–thermomechanical numerical modelling approach described in detail by Gerya *et al.* (2004a, 2006). In this approach all local rock properties, including effective density, isobaric heat capacity, thermal expansion, adiabatic and latent heating, are calculated at every time step based on Gibbs energy minimization.

Viscosity dependent on strain rate, pressure and temperature is defined in terms of deformation invariants (Ranalli 1995) as:

$$\eta_\mathrm{creep} = (\dot{\varepsilon}_{\mathrm{II}})^{(1-n)/2n}F(A_\mathrm{D})^{-1/n}$$
$$\times \exp\left(\frac{E_\mathrm{a} + V_\mathrm{a}P}{nRT}\right)$$

where $\dot{\varepsilon}_{\mathrm{II}} = 1/2\dot{\varepsilon}_{ij}\dot{\varepsilon}_{ij}$ is the second invariant of the strain rate tensor, and A_D, E_a, V_a and n are experimentally determined flow law parameters (Table 1). F is a dimensionless coefficient depending on the type of experiments on which the flow law is based. For example:

$$F = \frac{2^{(1-n)/n}}{3^{(1+n)/2n}} \quad \text{for triaxial compression}$$

$$F = 2^{(1-2n)/n} \quad \text{for simple shear.}$$

The ductile rheology is combined with a brittle–plastic rheology to yield an effective visco-plastic rheology. For this purpose the Mohr–Coulomb yield criterion (e.g. Ranalli 1995) is implemented by limiting creep viscosity, η_creep, as follows:

$$\eta_\mathrm{creep} \leq \frac{c + P\sin(\varphi)}{(4\dot{\varepsilon}_{\mathrm{II}})^{1/2}}$$

where P is the complete (non-lithostatic) pressure (i.e. the mean stress), c is the cohesion (residual strength at $P = 0$) and φ is effective internal friction angle (Table 1). Assuming high pore fluid pressure in hydrated rocks (e.g. Gerya *et al.* 2008a), the upper oceanic crust (basalts, sediments) was

characterized by $c = 1$ MPa, $\sin \varphi = 0$, a choice that effectively decouples the slabs. As the focus of our paper is viscous breakoff we assigned a high plastic strength to the mantle ($\sin \varphi = 0.6$: Brace & Kohlstedt 1980). Consequently, the plastic strength of subducted slabs in our experiments is always greater than the critical value (500 MPa) reported by Andrews & Billen (2009), and slab detachment occurs in the purely viscous mode by temperature- and stress-activated dislocation creep.

The effective viscosity, η, of molten crustal rocks at $P-T$ conditions above their wet solidus (Table 1) was lowered to 10^{19} Pa s. 10^{19} and 10^{26} Pa s are the lower and upper cut values for viscosity of all types of rocks in our numerical experiments.

Modelling results

Ten experiments (Table 2) were performed to study the influence of: (1) slab age; (2) plate rate; and (3) phase transitions on the dynamics of subduction. Numerical experiments were performed using the ETH-Zurich Brutus cluster.

Reference models development

In our two reference models (models cydc and cydd in Table 2) we distinguish five characteristic phases (Figs 2–4).

(a) Oceanic slab subduction and bending; this stage initiates with prescribed convergence rate but thereafter evolves self-consistently (Fig. 2a).

(b) Continental collision followed by slab blocking (due to the positive buoyancy of continental crust once it has been subducted to $100-125$ km depth), thermal relaxation and unbending; this stage consists of intense heat exchange between the subducted slab and the surrounding asthenospheric mantle Figs 2b, 3a & 4a); this stage is often manifest by slab decoupling from the overriding plate and asthenospheric upwelling due to the slab roll-back under the orogen (Fig. 4b, c). These latter processes are driven by the slab pull and are most pronounced in experiments with old (dense) oceanic plates (≥ 80 Ma, cf. Figs 2c & 3b). The bent slab is unbending under its own weight (Fig. 2b), which is also facilitated by the slab roll-back;

(c) Slab stretching and necking (Fig. 2c). Stretching of the slab is directly related to its thermal softening during the previous stage. The former ocean–continent boundary is subducted together with the stretching slab toward depths of more then 200 km; continental crust, however, continuously detaches from the slab and remains at shallower (≤ 100 km) levels beneath the orogen (Fig 2c).

(d) Viscous slab breakoff and rapid sinking (Figs 2d, 3b & 4c). This stage is similar to previous models of breakoff with prescribed slab blocking (Gerya *et al.* 2004b; Andrews & Billen 2009), except that the geometry of the collisional orogen formed at the plate contact evolves naturally with time allowing, in particular, for notable post-breakoff extension (cf. Fig. 4c, d) driven by the positive buoyancy of previously subducted continental crust.

(e) Post-breakoff relaxation; this stage is manifest by thermal and topographical relaxation of the orogen associated with exhumation and melting of previously subducted continental and oceanic crust located below the extending plate interface (cf. pink partially molten crustal rocks in Fig. 4d). Within $10-20$ Ma from the breakoff event $1-4$ km of surface uplift occurs in a $200-300$ km-wide area above the plate contact (cf. Fig. 4c, d), this uplift is comparable with that observed in previous numerical models (Buiter *et al.* 2002; Gerya *et al.* 2004b; Andrews & Billen 2009).

Influence of slab age

Experiments on the function of the age of the subducting oceanic plate (Table 3) show that the necking process occurs later in older slabs (Fig. 5). This behaviour is mainly caused by the variations in temperature structure of the subducting oceanic plate (Gerya *et al.* 2004b) and is characteristic of the viscous mode of breakoff (Andrews & Billen 2009) investigated in our study. In older (i.e. colder) slabs more time is necessary for thermal relaxation to increase temperature and reduce the slab viscosity. Since breakoff process is a direct consequence of the slab necking, the breakoff also correlates with age (Fig. 6).

The correlation between slab age and breakoff duration [i.e. the time elapsed between the beginning of slab necking (Fig. 2b) and separation (Fig. 2d)] is more complex (Fig. 7). Two domains are visible in Figure 7: a domain characteristic of young slabs (<50 Ma) and an area for mature slabs (>50 Ma). For young slabs breakoff duration increases with slab age and is related to the influence of the growing slab thermal thickness and strength, which slow the necking process. This trend inverts in old slabs owing to the increasing slab negative buoyancy, higher stresses and stronger thermomechanical feedback, respectively; effects that accelerate necking and breakoff (Gerya *et al.* 2004b).

Influence of relative plate rates

There is no significant effect on the time required for the onset of necking and breakoff when one plate
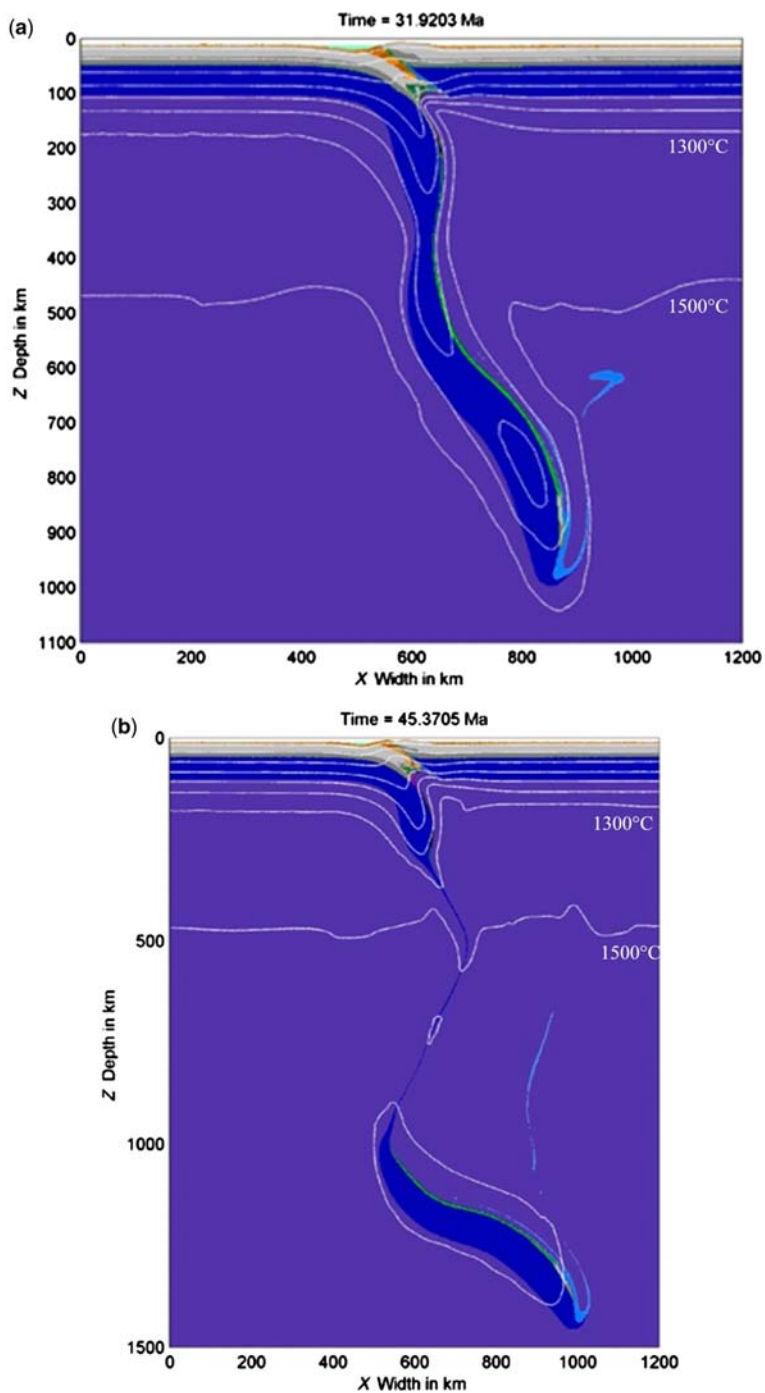
Fig. 3. Evolution of geometry and temperature of the detaching slab (Model cydc in Table 2). White lines are isotherms taken from 100 °C with 200 °C steps. (**a**) Slab stretching and beginning of necking process. (**b**) Slab breakoff and accelerated sinking.

C. BAUMANN *ET AL.*
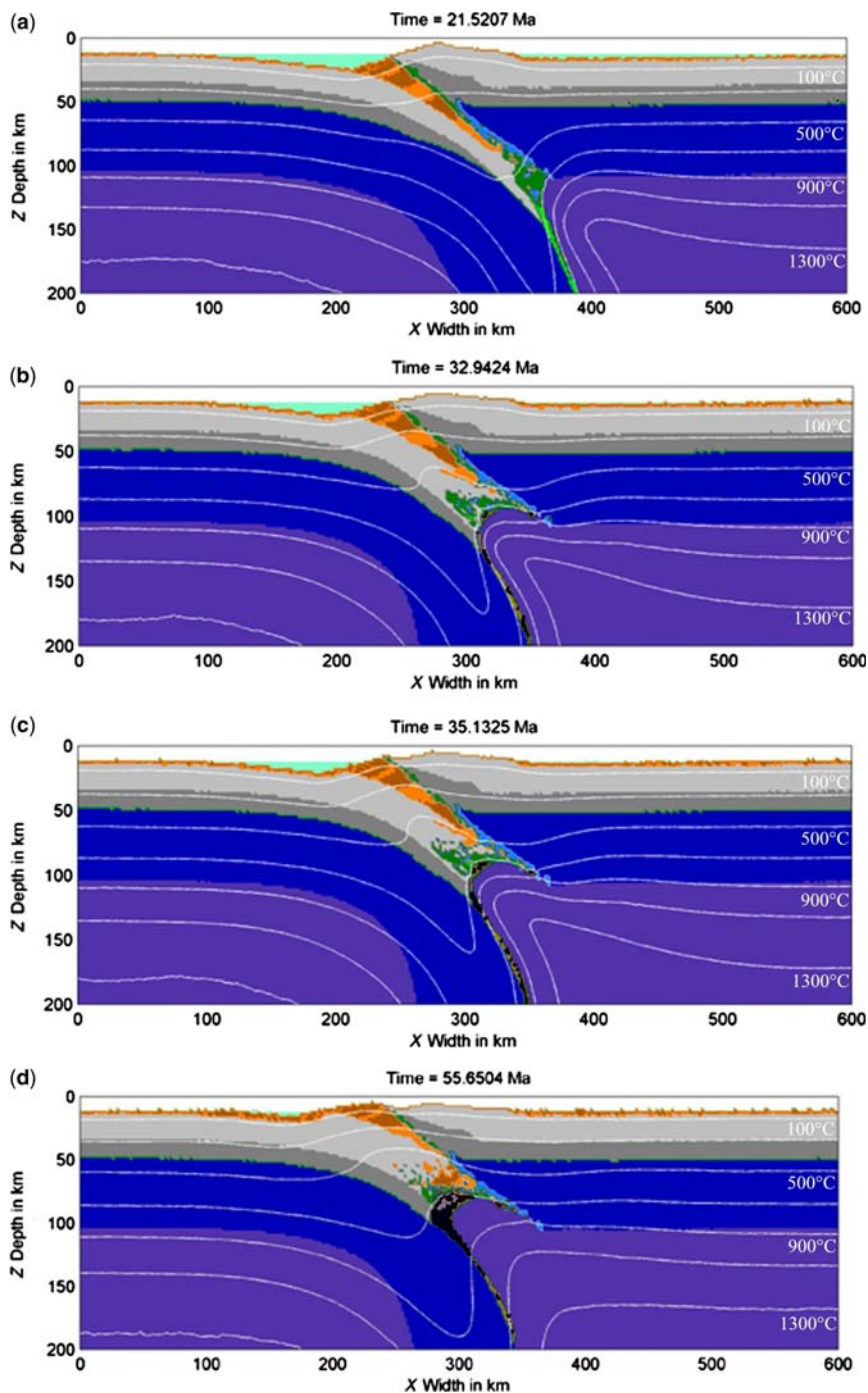
Fig. 4. Development of collision zone geometry during spontaneous slab breakoff process (Model cydc in Table 2). (**a**) Transition from subduction to collision; (**b**) beginning of necking process, slab roll-back associated with the opening of the asthenospheric window below the collision zone occurs; (**c**) time of breakoff; (**d**) post-breakoff time associated with exhumation and melting of deeply subducted crust. The black colour at the bottom of the subducted crust corresponds to partially molten crustal rocks. White lines are isotherms taken from 100 °C with 200 °C steps.

Table 3. *Influences of slab age*

| Name of the numerical experiment	Slab age (Ma)	Beginning of the necking process[1] (Ma)	Breakoff time[2] (Ma)	Breakoff duration[3] (Ma)	Breakoff depth[4] (km)
cyda	20	2.9708	6.1320	3.1612	406.780
cydb	40	12.6545	19.3235	6.6690	455.085
cydc	60	22.1207	28.5153	6.3946	444.915
cydd	80	33.2673	38.5978	5.3305	508.475
cyde	100	32.8012	35.4913	2.6901	432.203

[1]With beginning of the necking process meaning an observable necking of the subduted plate (Fig. 2c).
[2]Breakoff time means the moment of complete separation of the detached slab from the rest of the plate (Fig. 2d).
[3]The breakoff duration is the difference between the beginning of observable necking and complete slab separation.
[4]The depth where the separation and breakoff takes place (the deepest point of the separated plate isotherm).

velocity is adjusted in order to keep the total rate of convergence at 10 cm per year^{-1} (Table 4). This behaviour is to be expected because thermal structure of the slab is mainly affected by the total rate of convergence and not by relative plate velocities. In contrast, breakoff duration and depth (Table 4) are affected by relative plate rates. In particular, in our numerical experiments the duration of breakoff (Table 4) is shortest (5.3–5.7 Ma) when the velocities of both plates are similar in magnitude. The duration of breakoff is maximized (11.3 Ma) when the magnitude of the velocity of the overriding plate (10 cm year^{-1}) is much greater than that of the subducting plate (0 cm year^{-1}). Breakoff depth uniformly decreases with decreasing relative velocity of the subducting oceanic plate (Table 4). These variations in breakoff depth and duration are most probably caused by changing slab angle and curvature, which depend on the relative plate
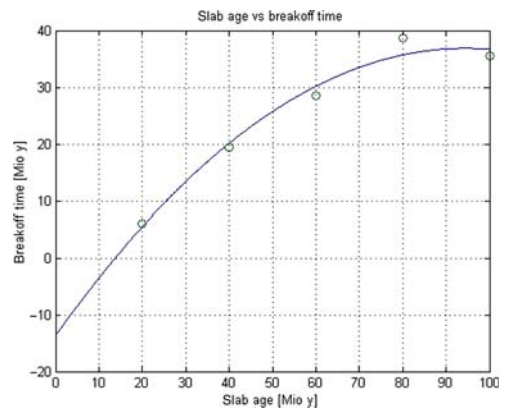
Fig. 6. Correlation between slab age and effective breakoff time. Symbols corresponds to numerical experiments. The line represents the best fit of numerical results with a second-order polynomial.
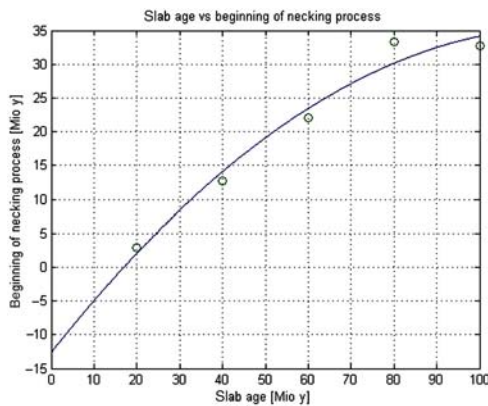
Fig. 5. Correlation between slab age and time (*t*) at the beginning necking process. Symbols correspond to numerical experiments. The line represents the best fit of numerical results with a second-order polynomial.
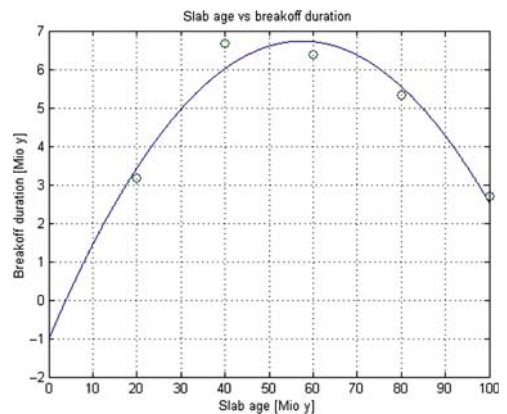
Fig. 7. Correlation between slab age and breakoff duration. Symbols correspond to numerical experiments. The line represents the best fit of numerical results with a second-order polynomial.

Table 4. *Influences of plate rate*

Name of the numerical experiment	Slab age (Ma)	Plate rates (cm year^{-1})		Beginning of the necking process (Ma)	Breakoff time (Ma)	Breakoff duration (Ma)	Breakoff depth (km)
		Left plate	Right plate				
cydd	80	+05	−05	33.2673	38.5978	5.3305	508.475
cyaq	80	+10	00	29.0926	35.7112	6.61860	562.500
cyar	80	00	−10	31.8691	43.2067	11.3376	460.169
cyas	80	+03	−07	33.1033	38.4074	5.30410	432.203

velocities; for exmaple, if the overriding plate is fast, the slab angle is shallower (van Hunen *et al.* 2000). In the model with the fastest overriding plate velocity (10 cm year^{-1}, model cyar in Tables 2 & 4) the slab is flattened at a depth of 660 km (e.g. Mishin *et al.* 2008), which is not observed in our reference model with a similar slab age (model cydd in Tables 2 & 4; Fig. 2). In contrast, in the model with the fastest subducting plate velocity (10 cm year^{-1}, model cyaq in Tables 2 & 4) the subducting slab is steeper and has stronger curvature than in the reference model (Fig. 2a).

Influence of phase transitions

In our experiments a fully coupled petrological–thermomechanical model based on Gibbs free energy minimization is used that accounts for both continuous and discontinuous phase transformations in the mantle and subducted oceanic crust (cf. Mishin *et al.* 2008 for details). The lowered temperatures in the descending oceanic plate cause it to have a different mineralogy and higher density than the surrounding mantle. Most significant, additional downwards body force on the descending slab is caused by the phase transition of olivine into spinel at a depth of about 410 km, which accelerates viscous detachment dynamics (Zlotnik *et al.* 2008). Further negative buoyancy effects may come from eclogitization of the subducted oceanic crust.

We ran two additional experiments without phase transitions for various slab ages (models cydh and cydi in Table 2). Results for pairs of models with and without phase transformations are compared in Table 5 and Figure 8. As follows from our comparison, phase transitions notably accelerate the breakoff process and increase the depth of slab breakoff (Fig. 8). These influences are obviously caused by the stronger negative buoyancy of the subducted slab affected by phase transitions. Consequently, in models with phase transitions the characteristic density contrast of the slab with the surrounding asthenospheric mantle is $100-200$ kg m^3, which is two–three times larger than the density contrast in models without phase transitions ($50-70$ kg m^{-3}).

Discussion and conclusions

In previous numerical studies (Gerya *et al.* 2004*b*; Zlotnik *et al.* 2008; Andrews & Billen 2009) the cessation of active subduction that is ultimately responsible for breakoff has been kinematically prescribed. The asset of our model is that it simulates both subduction and collision as dynamic processes. Specifically, our experiments model slab detachment induced by slab pull that develops owing to a continental collision after 700 km of oceanic plate subduction. During this latter stage the plate convergence rate evolves realistically (e.g. Chemenda *et al.* 2000; Faccenda *et al.* 2008). The chief limitation of our model is that the rheology includes neither elasticity (e.g. Buiter *et al.* 2002) nor Peierls plasticity (e.g. Kameyama *et al.* 1999). These deformation mechanisms may influence the transition from viscous to plastic detachment

Table 5. *Influences of phase transitions*

Numerical experiment	Beginning of the necking (Ma)	Time of breakoff (Ma)	Breakoff duration (Ma)	Breakoff depth (km)
cydc	22.1207	28.5153	6.3946	444.915
cydi (no phase transitions)	29.4116	34.7640	5.3524	330.508
cydb	12.6545	19.3235	06.6690	457.627
cydh (no phase transitions)	16.5099	36.2608	19.7509	317.790
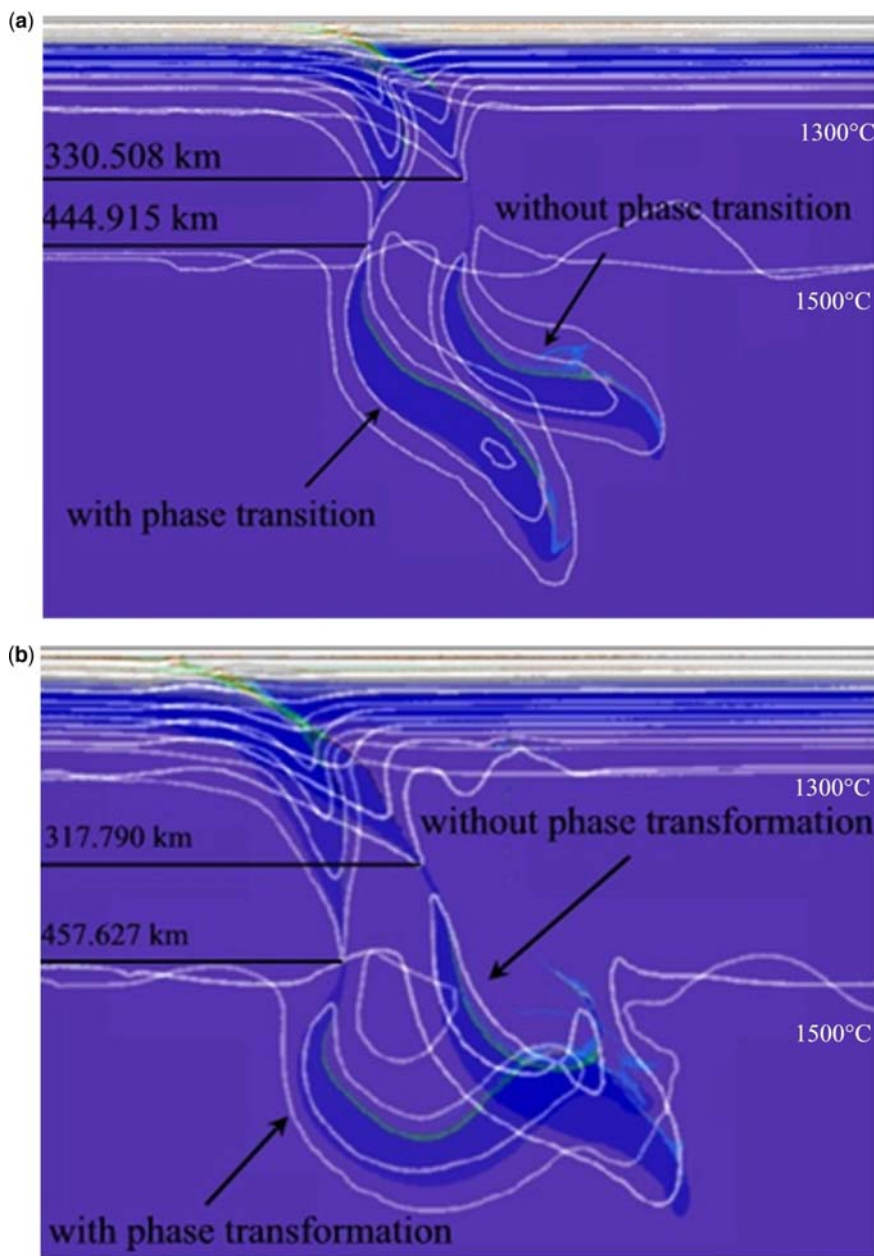
Fig. 8. Influence of phase transitions onto the depth of slab breakoff. (**a**) Model cydc compared with Model cydi. (**b**) Model cydb compared with Model cydh. The snapshots for different models are taken for different moments in time when breakoff occurs in each model (Table 5). White lines are isotherms taken from 100 °C with 200 °C steps.

(Andrews & Billen 2009) and the development of topography (Buiter *et al.* 2002). Additional limitations are the simplified rock chemistry and that the petrological model does not account for metastable phase assemblages which might occur in the subducted gabbroic crust (e.g. van Hunen *et al.* 2000) and lithospheric mantle (e.g. Schmelling *et al.* 1998). Thus, negative buoyancy of slabs in our experiments may be overestimated. In natural subduction settings significant along-strike

variations in the dynamics of breakoff processes are inferred from seismic and topographical data (e.g. Wortel & Spakman 1992, 2000). Such 3D effects cannot be accounted for by the present 2D model.

Five evolutionary phases occur in most of our experiments: (a) oceanic slab subduction and bending; (b) continental collision initiation followed by a cessation of subduction, thermal relaxation and unbending; (c) slab stretching and necking; (d) slab breakoff and sinking; and (e) post-breakoff relaxation.

The development of our dynamic thermomechanical model of continental collision has a number of similarities with previous analogue and numerical collision models that take into account significant buoyancy effects arising from continental crust subduction (e.g. Chemenda *et al.* 2000; Burov *et al.* 2001; Faccenda *et al.* 2008). In particular, our results confirm a positive correlation between the oceanic slab age and the time of necking and breakoff found in previous thermomechanical studies of the viscous mode of detachment, exploring models without phase transformations (Gerya *et al.* 2003; Andrews & Billen 2009). However, previous work did not report the non-linear dependence of breakoff duration on the slab age: a positive correlation being characteristic of relatively young (<50 Ma) slabs, while for older slabs the correlation is negative. We also found that at a constant convergence rate, a relatively high velocity of subducting oceanic plate increases the depth of breakoff, most probably because of the geometric consequences of the subducting plate (van Hunen *et al.* 2000) that influences the dynamics of phase transformations affecting slab buoyancy.

A prediction from our breakoff models is that the olivine–wadsleyite transition plays a role in localizing viscous slab breakoff at depths of 410–510 km owing to the buoyancy effects of the transition (e.g. Schmelling *et al.* 1998; Zlotnik *et al.* 2008). Without phase transitions, the slab is significantly less dense. The breakoff in this case is shallower, occurs later and lasts longer.

References

ANDREWS, E. R. & BILLEN, M. I. 2009. Rheologic controls on the dynamics of slab detachment. *In*: MCCRORY, P. & WILSON, D. (eds) *Interpreting the Tectonic Evolution of Pacific Run Margins Using Plate Kinematics and Slab Window Volcanism. Tectonophysics*, **464**, 60–69.

BARAZANGI, M., ISACKS, B. L., OLIVER, J., DUBOIS, J. & PASCAL, G. 1973. Descent of lithosphere beneath New Hebrides, Tonga–Fiji and New Zealand: evidence for detached slabs. *Nature*, **242**(5393), 98–101.

BRACE, W. F. & KOHLSTEDT, D. T. 1980. Limits on lithospheric stress imposed by laboratory experiments. *Journal of Geophysical Research*, **85**, 6248–6252.

BUITER, S. J. H., GOVERS, R. & WORTEL, M. J. R. 2002. Two-dimensional simulations of surface deformation caused by slab detachment. *Tectonophysics*, **354**, 195–210.

BUROV, E., JOLIVET, L., LE POURHIET, L. & POLIAKOV, A. 2001. A thermomechanical model of exhumation of high pressure (HP) and ultra-high pressure (UHP) metamorphic rocks in Alpine-type collision belts. *Tectonophysics*, **342**, 113–136.

CHEMENDA, A. I., BURG, J.-P. & MATTAUER, M. 2000. Evolutionary model of the Himalaya–Tibet system: geopoem based on new modelling, geological and geophysical data. *Earth and Planetary Science Letters*, **174**, 397–409.

CHOPRA, P. N. & PATERSON, M. S. 1981. The experimental deformation of dunite. *Tectonophysics*, **78**, 453–473.

CHUNG, W.-Y. & KANAMORI, H. 1976. Source process and tectonic implications of the Spanish deep-focus earthquake of March 29, 1954. *Physics of the Earth and Planetary Interiors*, **13**(2), 85–96.

CLAUSER, C. & HUENGES, E. 1995. Thermal conductivity of rocks and minerals, *In*: AHRENS, T. J. (ed.) *Rock Physics and Phase Relations*. American Geophysical Union, Reference Shelf, **3**, 105–126.

CONNOLLY, J. A. D. 2005. Computation of phase equilibria by linear programming: a tool for geodynamic modelling and an application to subduction zone decarbonation. *Earth and Planetary Science Letters*, **236**, 524–541.

DAVIES, J. H. & VON BLANCKENBURG, F. 1995. Slab breakoff: a model of lithospheric detachment and its test in the magmatism and deformation of collisional orogens. *Earth and Planetary Science Letters*, **129**, 85–102.

FACCENNA, C., BELIER, O., MARTINOD, J., PIROMALLO, C. & REGARD, V. 2006. Slab detachment beneath eastern Anatolia: a possible cause for the formation of the North Anatolian fault. *Earth and Planetary Science Letters*, **242**, 85–97.

FACCENDA, M., GERYA, T. V. & CHAKRABORTY, S. 2008. Styles of post-subduction collisional orogeny: Influence of convergence velocity, crustal rheology and radiogenic heat production. *Lithos*, **103**, 257–287.

FOWLER, C. M. R. 2005. *The Solid Earth*. Cambridge University Press, Cambridge.

FUCHS, K., BONJER, K.-P. *ET AL.* 1979. The Romanian earthquake of March 4, 1977: II, aftershocks and migration of seismic activity. *Tectonophysics*, **53**(3–4), 225–247.

GERYA, T. V. & YUEN, D. A. 2003*a*. Characteristics-based marker-in-cell method with conservative finite-differences schemes for modelling geological flows with strongly variable transport properties. *Physics of the Earth and Planetary Interiors*, **140**, 295–320.

GERYA, T. V. & YUEN, D. A. 2003b. Rayleigh–Taylor instabilities from hydration and melting propel cold plumes at subduction zones. *Earth and Planetary Science Letters*, **212**, 47–62.

GERYA, T. V., CONNOLLY, J. A. D., YUEN, D. A., GORCZYK, W. & CAPEL, A. M. 2006. Seismic implications of mantle wedge plumes. *Physics of the Earth and Planetary Interiors*, **156**, 59–74.

GERYA, T. V., CONNOLLY, J. A. D. & YUEN, D. A. 2008a. Why is terrestrial subduction onesided? *Geology*, **36**, 43–46.

GERYA, T. V., PERCHUK, L. L. & BURG, J.-P. 2008b. Transient hot channels: perpetrating and regurgitating ultrahigh-pressure, high temperature crust–mantle associations in collision belts. *Lithos*, **103**, 236–256.

GERYA, T. V., PERCHUK, L. L., MARESCH, W. V. & WILLNER, A. P. 2004a. Inherent gravitational instability of hot continental crust: implication for doming and diapirism in granulite facies terrains. *In*: WHITNEY, D., TEYSSIER, C. & SIDDOWAY, C. S. (eds) *Gneiss Domes in Orogeny*. Geological Society of America, Special Paper, **380**, 117–127.

GERYA, T. V., YUEN, D. A. & MARESCH, W. V. 2004b. Thermomechanical modelling of slab detachment. *Earth and Planetary Science Letters*, **226**, 101–116.

HIROSE, K. & FEI, Y. W. 2002. Subsolidus and melting phase relations of basaltic composition in the uppermost lower mantle. *Geochimica et Cosmochimica Acta*, **66**, 2099–2108.

IRIFUNE, T. & RINGWOOD, A. E. 1993. Phase transformations in subducted oceanic crust and buoyancy relationships at depths of 600–800 km in the mantle. *Earth and Planetary Science Letters*, **117**, 101–111.

IRIFUNE, T., RINGWOOD, A. E. & HIBBERSON, W. O. 1994. Subduction of continental crust and terrigenous and pelagic sediments: an experimental study. *Earth and Planetary Science Letters*, **126**, 351–368.

ISACKS, B. & MOLNAR, P. 1969. Mantle earthquake mechanisms and the sinking of the lithosphere. *Nature*, **223**(5211), 1121–1124.

KAMEYAMA, M., YUEN, D. A. & KARATO, S. 1999. Thermal–mechanical effects of low-temperature plasticity (the Peierls mechanism) on the deformation of a viscoelastic shear zone. *Earth and Planetary Science Letters*, **168**, 159–172.

KHAN, A., CONNOLLY, J. A. D. & OLSEN, N. 2006. Constraining the composition and thermal state of the mantle beneath Europe from inversion of long-period electromagnetic sounding data. *Journal of Geophysical Research*, **111**, B10102.

LARSEN, T. B., YUEN, D. A. & MALEVSKY, A. V. 1995. Dynamical consequences on fast subducting slabs from a self-regulating mechanism due to viscous heating in variable viscosity convection. *Geophysical Research Letters*, **22**, 1277–1280.

LEVIN, V., SHAPIRO, N., PARK, J. & RITZWOLLER, M. 2002. Seismic evidence for catastrophic slab loss beneath Kamchatka. *Nature*, **418**, 763–767.

MISHIN, Y. A., GERYA, T. V., BURG, J.-P. & CONNOLLY, J. A. D. 2008. Dynamics of double subduction: numerical modeling. *Physics of the Earth and Planetary Interiors*, **171**, 280–295.

ONO, S., OHISHI, Y., ISSHIKI, M. & WATANUKI, T. 2005. *In situ* X-ray observations of phase assemblages in peridotite and basalt compositions at lower mantle conditions: implications for density of subducted oceanic plate. *Journal of Geophysical Research*, **110**, B02208.

PASCAL, G., DUBOIS, J., BARAZANGI, M., ISACKS, B. L. & OLIVER, J. 1973. Seismic velocity anomalies beneath the New Hebrides island arc: evidence for a detached slab in the upper mantle. *Journal of Geophysical Research*, **78**(29), 6998–7004.

POLI, S. & SCHMIDT, M. W. 2002. Petrology of subducted slabs. *Annual Review of Earth and Planetary Sciences*, **30**, 207–235.

PYSKLYWEC, R. N., BEAUMONT, C. & FULSACK, P. 2000. Modeling the behavior of the continental mantle lithosphere during plate convergence. *Geology*, **28**, 655–658.

PYSKLYWEC, R. N. 2006. Surface erosion control on the evolution of the deep lithosphere. *Geology*, **34**, 225–228.

RANALLI, G. 1995. *Rheology of the Earth*. Chapman & Hall, London.

REGENAUER-LIEB, K., YUEN, D. A. & BRANLUND, J. 2001. The initiation of subduction: criticality by addition of water? *Science*, **294**, 578–580.

SACKS, P. E. & SECOR, D. T. 1990. Delamination in collisional orogens. *Geology*, **18**, 999–1002.

SCHMELLING, H., BABEYKO, A. Y. *ET AL*. 2008. A benchmark comparison of spontaneous subduction models – Towards a free surface. *Physics of the Earth and Planetary Interiors*, **171**, 198–223.

SCHMELLING, H., MONZ, R. & RUBIE, D. C. 1998. The influence of olivine metastability on the dynamics of subduction. *Earth and Planetary Science Letters*, **165**, 55–66.

SCHMIDT, M. W. & POLI, S. 1998. Experimentally based water budgets for dehydrating slabs and consequences for arc magma generation. *Earth and Planetary Science Letters*, **163**, 361–379.

SOBOLEV, S. V. & BABEYKO, A. Y. 2005. What drives orogeny in the Andes? *Geology*, **33**, 617–620.

SPAKMAN, W., WORTEL, M. J. R. & VLAAR, N. J. 1988. The Hellenic subduction zone: a tomographic image and its geodynamic implications. *Earth and Planetary Science Letters*, **15**, 60–63.

STIXRUDE, L. & BUKOWINSKI, M. S. T. 1990. Fundamental thermodynamic relations and silicate melting with implications for the constitution of D''. *Journal of Geophysical Research*, **95**, 19,311–19,325.

STIXRUDE, L. & LITHGOW-BERTELLONI, C. 2005. Mineralogy and elasticity of the oceanic upper mantle: origin of the low-velocity zone. *Journal of Geophysical Research*, **110**, B03204.

TURCOTTE, D. L. & SCHUBERT, G. 2002. *Geodynamics*. Cambridge University Press, Cambridge.

UEDA, K., GERYA, T. V. & SOBOLEV, S. 2008. Subduction initiation by thermal–chemical plumes: numerical studies. *Physics of the Earth and Planetary Interiors*, **171**, 296–312.

VANCE, D., BICKLE, M., IVY-OCHS, S. & KUBIK, P. W. 2003. Erosion and exhumation in the Himalaya from cosmogenic isotope inventories of river sediments. *Earth and Planetary Science Letters*, **206**, 273–288.

VAN HUNEN, J., VAN DEN BERG, A. P. & VLAAR, N. J. 2000. A thermomechanical model of horizontal

subduction below an overriding plate. *Earth and Planetary Science Letters*, **182**, 157–169.

VON BLANCKENBURG, F. & DAVIES, J. H. 1995. Slab breakoff: a model for syncollisional magmatism and tectonics in the Alps. *Tectonics*, **14**, 120–131.

WONG A TON, S. Y. M. & WORTEL, M. J. R. 1997. Slab detachment in continental collision zones: an analysis of controlling parameters. *Geophysical Research Letters*, **24**(16), 2095–2098.

WORTEL, M. J. R. & SPAKMAN, W. 1992. Structure and dynamics of subducted lithosphere in the mediterranean region. *Proceedings of the Koninklijke Nederlandse Akademie van Wetenschappen*, **95**, 325–347.

WORTEL, M. J. R. & SPAKMAN, W. 2000. Geophysics – subduction and slab detachment in the Mediterranean–Carpathian region. *Science*, **290**, 1910–1917.

XU, P. F., SUN, R. M., LIU, F. T., WANG, Q. & CONG, B. 2000. Seismic tomography showing, subduction and slab breakoff of the Yangtze block beneath the Dabie–Sulu orogenic belt. *Chinese Science Bulletin*, **45**, 70–74.

YOSHIOKA, S. & WORTEL, M. J. R. 1995. Three-dimensional numerical modeling of detachment of subducted lithosphere. *Journal of Geophysical Research*, **100**, 20,233–20,244.

YOSHIOKA, S., YUEN, D. A. & LARSEN, T. B. 1995. Slab weakening: thermal and mechanical consequences for slab detachment. *Island Arc*, **40**, 89–103.

ZLOTNIK, S., FERNANDEZ, M., DIEZ, P. & VERGES, J. 2008. Modelling gravitational instabilities: slab break-off and Rayleigh–Taylor diapirism. *Pure and Applied Geophysics*, **165**, 1491–1510.